DEPARTMENT OF PHYSICS

ATMOSPHERIC, OCEANIC AND PLANETARY PHYSICS

A SEA SURFACE REFLECTANCE MODEL SUITABLE FOR USE WITH AATSR AEROSOL RETRIEVAL

A. Sayer
AOPP, University of Oxford

AOPP Memorandum 2007.2

January 2007

University of Oxford

Abstract

This document describes an algorithm for the calculation of sea surface reflectance, suitable for use in an AATSR aerosol retrieval. Methods used in, for example, the 6S model of Vermote et al. [1997], from which this one is derived, are typically concerned with the region from 400 nm to 700 nm. AATSR's visible channels are from 550 nm to 1.6 μm, hence new values of parameters must be researched, and previous assumptions re-evaluated, to create an model suitable for AATSR. Some examples of aerosol retrieval using the new surface algorithm are also presented.

Contents

1 Definition and components of reflectance

1.1 Definition of terms

The reflectance of a body, denoted here by the letter ρ, is defined as the ratio of outgoing to incoming irradiance. Hence a perfectly white body has a reflectance of 1, and a perfectly black body a reflectance of 0, and it is a dimensionless quantity. Reflectance may be parametrised in terms of the following factors:

- Solar zenith angle θ_s (measured from vertical) and azimuth angle ϕ_s (measured from north).
- Viewing zenith angle θ_v (measured from vertical) and azimuth angle ϕ_v (measured from north).
- Relative azimuth angle, $\phi_r = \phi_s - \phi_v$.
- Wavelength, λ.
- Complex refractive index, $\tilde{n} = n - i\kappa$ with real component n and extinction coefficient κ.
- Wind speed w, measured in ms^{-1}.
- Wind direction. Rotating clockwise from north by the wind azimuth ϕ_w, we define $\chi = \phi_s - \phi_w$.
- The total concentration C of chlorophyll a and pheophytin a, measured in mg m^{-3}.

A reflectance is directional; it depends on the local solar and observational conditions. The reflectance may be integrated over all observation zenith and relative azimuth angles for a given solar angle to define a so-called *black sky albedo*; this represents the reflectance of the hemisphere of the surface with respect to a direct incoming beam of light. This can be further integrated over all solar angles to yield a *white sky albedo*, also called the *Lambertian* or *bihemispherical* albedo. This is independent of both viewing and solar geometries, and represents the isotropic reflectance of the surface to diffuse light. The current ORAC scheme assumes an underlying Lambertian surface.

1.2 The three components of ρ

The total reflectance ρ is defined by Koepke [1984] as being composed of three terms, representing three different sources of upwelling irradiance. Firstly, light can be reflected off whitecaps in the rough ocean surface; secondly, it can be reflected off the darker surface itself. The relative contributions from these two factors will depend on the roughness of the sea surface, which is dependent on the wind speed. Thirdly, light penetrating the surface can be scattered back up into the atmosphere by molecules within the water, such as water and dissolved pigments. Considering the combination of these terms, we arrive at the following relationship:

$$\rho = W\rho_{wc} + (1-W)\rho_{gl} + (1-\rho_{wc})\rho_{ul} \tag{1}$$

In the above ρ_{wc} is the contribution from whitecaps; ρ_{gl} the contribution from sun glint; and ρ_{ul} the underlight term from radiance emitted just below the surface of the water. The parameter W is the fractional cover of whitecaps, described in the following chapter. Each of these three contributions is

dealt with separately here.

ρ_{gl} is weighted against by a factor of (1-W) as specular reflection is only possible where there are not whitecaps. Similarly, ρ_{ul} is weighted by a factor of (1-ρ_{wc}) because light reflected by whitecaps cannot be re-reflected as underlight. ρ_{ul} also includes a correction to account for light lost due to glint reflection at the surface; this will be dealt with in more detail in Chapter 4.

1.3 Typical values of reflectance

Results from this model indicate that the directional reflectance of the sea is highly variable with geometry, wind, wavelength and concentrations of dissolved pigments. The contributions of terms described in Equation 1 differ as parameters change, as will be discussed in succeeding sections, but in general the sea surface is brightest at shorter wavelengths (particularly in cases of low wind, where the underlight term dominates).

Typical values for a satellite zenith angle of 10°, solar zenith angle of 35°, relative azimuth angle and relative wind azimuth of 0°, wind speed of 5 ms^{-1} and pigment concentration of 0.3 mg m^{-3} are 0.0154 at 550 nm, 0.00382 at 670 nm, 0.00287 at 870 nm and 0.00267 at 1.6 μm.

2 Whitecaps

Whitecaps are where the ocean appears white due to the action of wind creating a foam. Probably the most simple of the three components of reflectance, their only dependence is on wind speed and wavelength.

2.1 Calculation

From Equation 1, the contribution of whitecaps to reflectance is the product of the proportion W of the surface covered by whitecaps and their average reflectance ρ_{wc}. Older work such as Koepke [1984] treated foam reflectance in the visible region as constant with wavelength, although noted that in the near-infrared it might be expected to decrease due to absorption by water molecules. More recent coastal work by Frouin et al. [1996], followed by work in the open ocean by Nicolas et al. [2001], suggests that there is, in fact, a decrease of about 40% at 850 nm and 85% at 1.65 μm, with a reflectance of about 0.4 at shorter wavelengths. These ratios have been adopted here for use at the nearby AATSR visible channel wavelengths, with reflectance at 550 nm and 660 nm assumed equal to 0.4.

The whitecap fraction W is here parametrised by in terms of wind speed by a simple power law according to the method of Monahan and Muircheartaigh [1980]. This is stated to hold for water warmer than 14°C but is here used for all waters. According to this method, and with the caveat that W cannot be greater than 1, the fraction of whitecaps is given by:

$$W = 2.951 \times 10^{-6}.w^{3.52} \tag{2}$$

It should be noted that determination of W is in general quite complicated, and various different parametrisations based on wind speed, and other environmental factors, have been developed. An overview of some of these methods is given by Anguelova and Webster [2006]. The method of Monahan and Muircheartaigh [1980] is currently being used as it has been widely-adopted (for example by Koepke [1984] and more recently Vermote et al. [1997]).

2.2 Magnitude of contribution

Wind speed w, ms^{-1}	Whitecap fraction W	Contribution to albedo at 0.55 μm $W \times \rho_{wc}$
0	2.951×10^{-6}	1.18×10^{-6}
5	8.23×10^{-4}	3.29×10^{-4}
10	9.77×10^{-3}	3.91×10^{-3}
15	1.96×10^{-2}	7.84×10^{-3}
20	1.12×10^{-1}	4.48×10^{-2}
25	2.46×10^{-1}	9.84×10^{-2}

Table 1: Values of W and $W \times \rho_{wc}$, the whitecap fraction and contribution to sea surface albedo at 0.55 μm, calculated for a range of representative wind speeds w.

The contribution of whitecap reflectance to ρ for several wind speeds is tabulated in Table 1. At low wind speeds this contribution–and associated whitecap fraction W–is small, although for wind speeds of 10 ms^{-1} and higher the whitecap fraction and contribution to albedo are considerable.

2.3 Uncertainties

There are several problems and sources of uncertainty with this section of the algorithm, which may need further exploration:

- There is a large uncertainty of up to 50% in the reflectance ρ_{wc} of foam, which will map into a corresponding uncertainty into their contribution to albedo.
- The expression used to calculate W from wind speed is one of many different parametrisations, and almost certainly too simple to accurately model the whitecap fraction. Reference to the source data for many of the different methods presented by Anguelova and Webster [2006] reveals a lot of scatter about the best-fit lines.
- Although high wind speeds are very unlikely, whitecap fraction will exceed 1 with winds of approximately 37 ms^{-1} or higher. The expression, then, provides unphysical values at high wind speeds.
- The expression used is mentioned as valid for water warmer than 14°C; an avenue of investigation would be how frequently parts of the sea are cooler than this, and how different the resulting expressions are.

2.4 Comparison with current algorithm

The algorithm currently in use for sea surface reflectance does not take account of oceanic whitecaps.

3 Glint reflectance

The contribution ρ_{gl} results from rays of light striking the sea surface and being reflected in the observer's direction. It is calculated using the Fresnel equations, modified to account for the roughness of the wind-ruffled sea surface according to statistics developed by Cox and Munk [1954*a*] (see also 1954*b*). More complicated than ρ_{wc}, ρ_{gl} depends on the following parameters:

- Solar zenith angle θ_s (measured from vertical) and azimuth angle ϕ_s (measured from north).
- Viewing zenith angle θ_v (measured from vertical) and azimuth angle ϕ_v (measured from north).
- Relative azimuth angle, $\phi_r = \phi_s - \phi_v$.
- Wavelength, λ.
- Real component n of refractive index.
- Wind speed w, measured in ms^{-1}.
- Wind direction. Rotating clockwise from north by the wind azimuth ϕ_w, we define $\chi = \phi_s - \phi_w$.

3.1 Calculation

3.1.1 Slope distribution

The algorithm defines a coordinate system (P, X, Y, Z) such that P is the observed point on the surface and Z the altitude with PY in the direction of the Sun and PX in the direction perpendicular to the Sun's plane. The surface slope is defined by the following two components:

$$Z_x = \frac{\partial Z}{\partial X} = \sin(\alpha)\tan(\beta) \tag{3}$$

$$Z_y = \frac{\partial Z}{\partial Y} = \cos(\alpha)\tan(\beta) \tag{4}$$

In the above α is the azimuth of the ascent (clockwise from the Sun) and β the tilt. Z_x and Z_y are related to the incident and reflected directions as follows, where $\theta_s < \pi/2$ and $\theta_v > 0$:

$$Z_x = \frac{-\sin(\theta_v)\sin(\phi)}{\cos(\theta_s) + \cos(\theta_v)} \tag{5}$$

$$Z_y = \frac{\sin(\theta_s) + \sin(\theta_v)\cos(\phi)}{\cos(\theta_s) + \cos(\theta_v)} \tag{6}$$

In reality, the slope distribution will be anisotropic and dependent on wind direction χ. We can rotate the axes clockwise from the north by χ to define a new coordinate system (P, X', Y', Z) where PY' is parallel to the wind direction. Then the slope components may be re-expressed:

$$Z'_x = \cos(\chi)Z_x + \sin(\chi)Z_y \tag{7}$$

$$Z'_y = \sin(\chi)Z_x + \cos(\chi)Z_y \tag{8}$$

The slope distribution is described by a Gram-Charlier series:

$$\begin{aligned} P(Z'_x, Z'_y) = & \frac{1}{2\pi\sigma'_x\sigma'_y} e^{(-\frac{\zeta^2+\eta^2}{2})} \big[1 - \frac{1}{2}\mathrm{C}_{21}(\zeta^2 - 1) \\ & - \frac{1}{6}\mathrm{C}_{03}(\eta^2 - \eta) + \frac{1}{24}\mathrm{C}_{40}(\zeta^4 - 6\zeta^2 + 3) \\ & + \frac{1}{4}\mathrm{C}_{22}(\zeta^2 - 1)(\eta^2 - 1) + \frac{1}{24}\mathrm{C}_{04}(\eta^4 - 6\eta^2 + 3)\big] \end{aligned} \tag{9}$$

Terms in this series come from Cox and Munk [1954*b*] and, for a clean surface, are defined as follows:

- $\zeta = Z'_x/\sigma'_x$ and $\eta = Z'_y/\sigma'_y$ where σ'_x and σ'_y are the root mean square values of Z'_x and Z'_y respectively. The value of σ'^2_x is given as $0.003 + 0.00192w \pm 0.002$ and $\sigma'^2_y = 0.00316w \pm 0.004$.
- C_{21} and C_{03} are the skewedness coefficients. These have values of $0.01 - 0.0086w \pm 0.03$ and $0.04 - 0.033w \pm 0.12$ respectively.
- C_{40}, C_{22} and C_{04} are the peakedness coefficients. These have values of 0.40 ± 0.23, 0.12 ± 0.06 and 0.23 ± 0.41 respectively.

3.1.2 The Fresnel reflection coefficient

The Fresnel reflection coefficient R describes the proportion of light hitting the surface that is reflected back. Vermote et al. [1997] provide a method to calculate this and refer to the *Optics of metals* section of Born and Wolf [1975]. Cox and Munk [1954*a*] themselves provided a method to compute R, which is simpler than the former. It neglects the complex part of the index of refraction (probably a valid approximation because this is a small term, as shown in Table 2). For unpolarised light, R is defined as follows:

$$R = \frac{1}{2}\left(\left[\frac{\sin(\omega - \omega')}{\sin(\omega + \omega')}\right]^2 + \left[\frac{\tan(\omega - \omega')}{\tan(\omega + \omega')}\right]^2\right) \tag{10}$$

Here ω is the scattering angle–the angle of the incident ray to the surface (and angle of reflection from it), while ω' is the angle of the refracted ray passing into the water, as shown in Figure 1. Snell's Law describes the relationship between these angles:

$$n_{air}\sin\omega = n_{water}\sin\omega' \tag{11}$$

The real component of the refractive index of air, n_{air}, is taken as 1.00029 for all wavelengths. The refractive index of water varies with wavelength; values from Hale and Querry [1971] as shown in Table 2 are used. An additional correction of +0.006 (not shown in the table) is added to the real component due to the salinity and chlorinity of typical seawater.

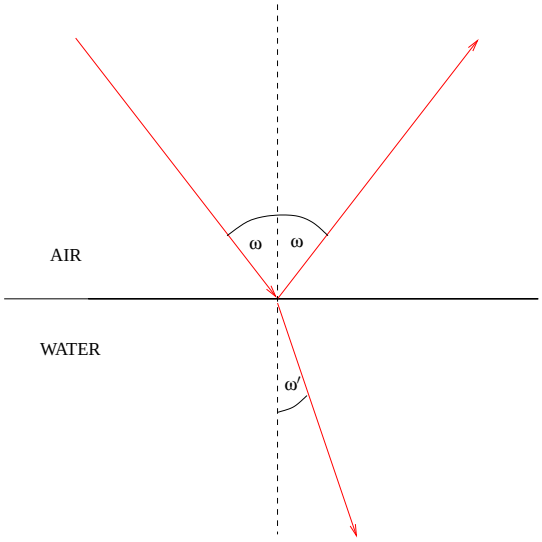

Figure 1: Geometry of Fresnel reflectance: the angle ω is the angle of incidence to the surface and angle of reflection from it, both measured relative to the normal. ω' is the angle of the refracted beam in the water. As water has a higher refractive index than air, by Snell's Law $\omega > \omega'$. Red lines represent the paths of light rays.

The angle ω can be calculated from Equations 3, 4, 5 and 6, and is described in the α and β coordinate system by Cox and Munk [1954*a*]. The following result can be obtained, in terms of our known values θ_s and θ_v, which indirectly provides ω:

$$\cos(2\omega) = \cos(\theta_v)\cos(\theta_s) + \sin(\theta_v)\sin(\theta_s)\cos(\phi_r) \tag{12}$$

From this and the previous equations R may be calculated at the wavelengths of interest.

3.1.3 Combination of terms

The total contribution ρ_{gl} is given by the following equation:

Wavelength λ	Real component n	Imaginary component κ
550 nm	1.333	1.96×10^{-9}
675 nm	1.331	2.23×10^{-8}
875 nm	1.328	3.91×10^{-7}
1.6 μm	1.317	8.55×10^{-5}

Table 2: Refractive indices $\tilde{n}$ for water from Hale and Querry [1971] at wavelengths near AATSR visible channels. Both real n and imaginary κ components are given, although only the real part is used in determining the Fresnel coefficient.

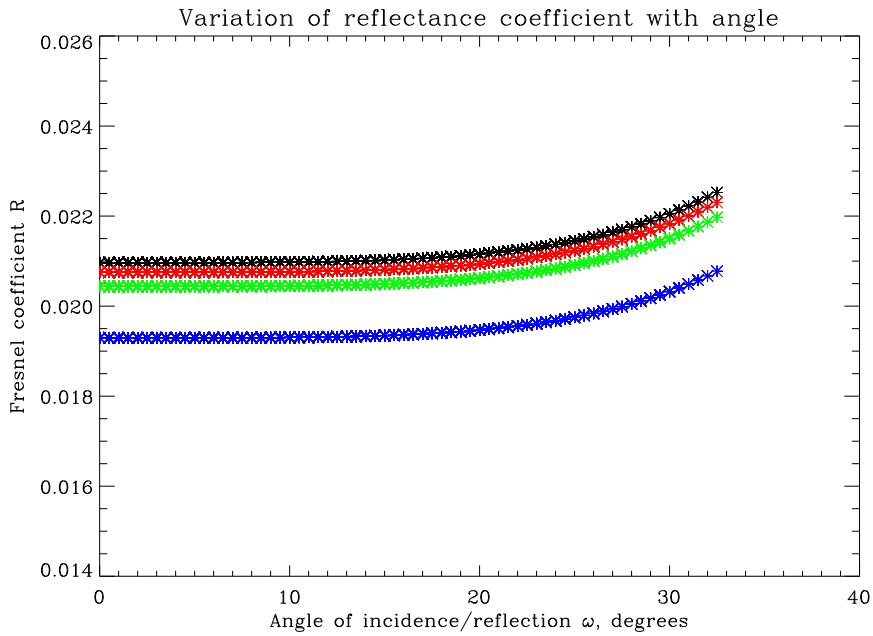

Figure 2: Variation of the Fresnel reflection coefficient R with ω, the angle of incidence and reflection to the normal of the surface. Black is 550 nm, red 660 nm, green 870 nm and blue 1.6 μm.

$$\rho_{gl} = \frac{\pi P(Z'_x, Z'_y) R}{4\cos(\theta_s)\cos(\theta_v)\cos^4(\beta)} \tag{13}$$

The tilt β may be calculated from:

$$\cos(\beta) = \frac{\cos(\theta_s) + \cos(\theta_v)}{\sqrt{2 + 2\cos(2\omega)}} \tag{14}$$

3.2 Magnitude of contribution

The glint reflectance is strongly dependent on geometry and wind speed. Over the range of ω sampled (from 0 to around 32°), the reflection coefficient R shows little variation and a reasonably constant spectral shape. This is shown in Figure 2. P values, however, vary sharply with wind speed: for very low winds P is of the order 10^{-3}, leading to a very low ρ_{gl}, although for winds of about 5 ms^{-1} or more it is around 1. This means that ρ_{gl} will be lower than R, as is visible from Figure 3. The presence of multiple points at the same ω but different ρ_{gl} is due to the geometry dependence of Equation 13. Similarly, the data in the figure to not appear to sample the entire range of ω values from Figure 2 for the low-wind case because the resultant ρ_{gl} is smaller than 10^{-5}, the minimum increment of albedo in the AATSR retrieval.

In summary, the magnitude of ρ_{gl} can vary widely, from 10^{-5} and lower to around 10^{-2}. Where there is wind, common values are in the region 10^{-4} to 10^{-2}. There is a weak dependence on wavelength, approximately consistent over the angles sampled.

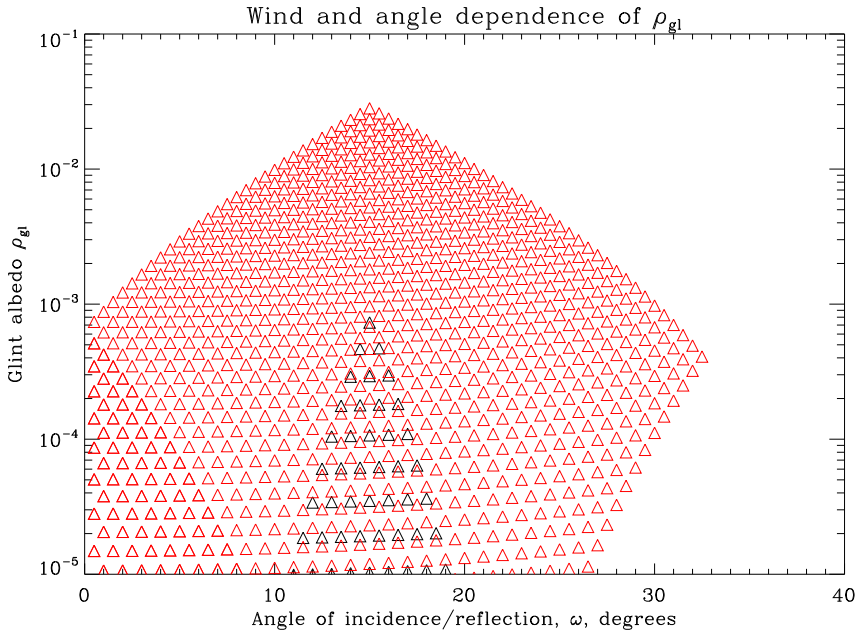

Figure 3: Variation of ρ_{gl} with ω (angle of incidence and reflection to the normal of the surface) and wind speed. Black triangles represent values for a wind speed of 1 ms^{-1} while red are for 10 ms^{-1}. The wavelength is 550 nm in both cases.

3.3 Uncertainties

The coefficients used in the Gram-Charlier series have a large uncertainty, although the influence of this on P is probably fairly small, particularly with wind speeds on the order of 10 ms^{-1} or higher. This is unlikely to be something that can be improved on.

3.4 Comparison with current algorithm

The current algorithm in use calculates ρ_{gl} as the sole contribution to reflectance, and the method is fairly similar overall. There are three points of note:

- The current algorithm appears to use an exponential decay function, as opposed to a Gram-Charlier series, to calculate the slope distribution P.
- Reference is made by the current algorithm to a correction to β made by Zeisse, although no explicit publication is mentioned in the code. The correction is made to improve the approximations when θ_v is larger than 70°–it is probably not necessary, as the largest θ_v encountered for AATSR is approximately 55°.
- In the calculation of R, the current algorithm uses not the standard Fresnel equation but the method of Sidran [1981]. Sidran's computation makes use of the complex permittivity of water, derived from refractive index. Results obtained are noticeably different from those using the standard Fresnel formula (Equation 10). The reasons for the difference are uncertain. Sidran's work is along the lines of Born and Wolf [1975], who use a more complicated form of the

Fresnel equations to deal with complex refractive indices (the imaginary parts of which, as discussed, are very small in this case).

It should be noted that the reflectance defined by Equation 13 is what is taken as equivalent to the Lambertian albedo for the ORAC retrieval at present. Due to its geometric dependence, however, it is not a true Lambertian description of the surface.

4 Underlight

Underlight is upwelling irradiance from just below the surface of the ocean. As such, ρ_{ul} is influenced directly by the following factors:

- Solar zenith angle θ_s (measured from vertical) and azimuth angle ϕ_s (measured from north).
- Viewing zenith angle θ_v (measured from vertical) and azimuth angle ϕ_v (measured from north).
- Wavelength, λ.
- Complex refractive index, $\tilde{n} = n - i\kappa$ with real component n and extinction coefficient κ.
- The total concentration C of chlorophyll a and pheophytin a, measured in mg m^{-3}.

4.1 Calculation

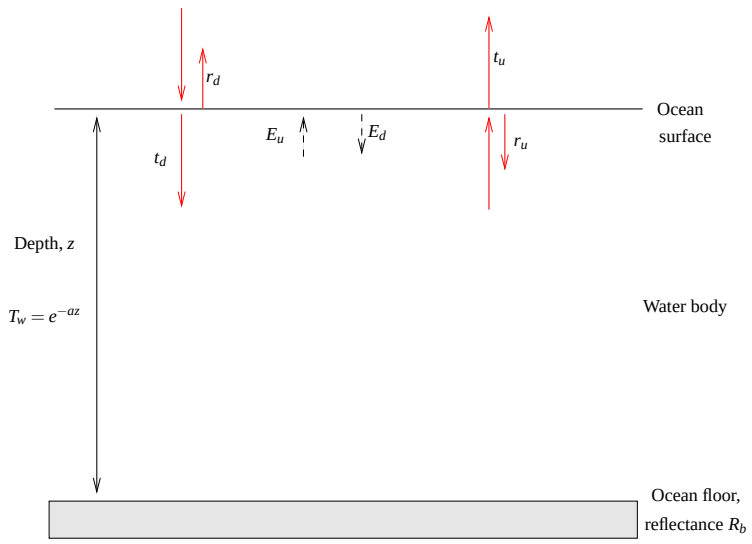

Figure 4: Terms important in calculation of underlight. Red lines represent light rays.

The underlight contribution may calculated using the method presented by Austin [1974], with the work begun in Morel and Prieur [1977] and further in Morel and Gentili [1991] for calculation of the water body reflectance R_w. The upwelling irradiance ρ_{ul} is described by the following equation:

$$\rho_{ul} = \frac{1}{n^2} \frac{t_d t_u (R_w + \frac{T_w^2 R_b}{1 - R_w R_b})}{1 - \bar{r}_u (R_w + \frac{T_w^2 R_b}{1 - R_w R_b})} \tag{15}$$

The factor of n^{-2} arises as the flux from a solid angle underneath the surface is refracted over a larger solid angle above it. The various parameters t_d, the transmittance coefficient for downwelling

radiation at the surface, r_d, the reflectance coefficient for downwelling radiation at the surface, t_u, the transmittance coefficient for upwelling radiation at the surface, $\bar{r_u}$ the mean value of r_u, the reflectance coefficient over all observation angles for upwelling radiation at the surface, and R_w, the water body reflectance, are described in succeeding sections of this document. It should be noted that $t_d + r_d = 1$ and $t_u + r_u = 1$; by conservation of energy, light is either transmitted or reflected. The parameters T_w and R_b are the transmittance through the body of water and the reflectance of the bottom of the sea respectively. These terms are visually represented in Figure 4.

Several approximations may be made involving these last two terms. Firstly, as R_w is likely to be small (discussed in Section 4.1.4) and R_b is necessarily less than 1 we may approximate that $R_w R_b$ is very small, and the denominators of Equation 15 where the term appears will be very close to 1. Secondly, the transmittance T_w may be calculated as follows:

$$T_w = e^{-a_w z} \tag{16}$$

In the above a_w is the absorption coefficient of the water, and z the depth. For pure water, a_w can be calculated from the complex part of the refractive index:

$$a_w = \frac{4\pi}{\lambda}\kappa \tag{17}$$

Values of κ were tabulated in Table 2 and, assuming pure water, may be used to calculate a_w and hence T_w for a variety of depths. Over all wavelengths of interest, and even in shallow water (with $z = 100$ m), the transmittance T_w is very small (with a maximum of 10^{-2} for $z = 100$ m at 550 nm, and orders of magnitude smaller for deeper water or longer wavelengths). It should be emphasised that these calculations are for pure water, and substances in seawater would further decrease T_w. As a result, $T_w^2 R_b$, the proportion of light transmitted through the water, reflected off the bottom and then transmitted up through the water body, may be neglected as almost zero. Then, with the first approximation of $R_w R_b$ being small, Equation 15 may be simplified as follows:

$$\rho_{ul} = \frac{1}{n^2}\frac{t_d t_u R_w}{1 - \bar{r_u} R_w} \tag{18}$$

This is the expression used to calculate ρ_{ul} in this scheme.

4.1.1 Downwelling transmittance coefficient, t_d

The term t_d in Equation 18 represents the transmittance of downwelling radiation, and assuming a Lambertian ocean may be calculated as follows:

$$t_d = 1 - \int_0^{2\pi}\int_0^{\pi/2} R_{aw}(\theta_s, \theta_d, \phi)\cos(\theta_d)\sin(\theta_d)\, d\theta_d\, d\phi \tag{19}$$

In the above, θ_d represents the zenith angle of a solar beam reflected from the rough water surface. As integration is carried out over all θ_d and azimuth angles ϕ this quantity is dimensionless. The coefficient R_{aw} is the Fresnel reflection coefficient for a ray incoming in at zenith angle θ_s and reflected at θ_d with relative azimuth angle ϕ between them. R_{aw} is calculated as described in Section 3.1.2, using θ_d for θ_v and ϕ for ϕ_r in Equation 12.

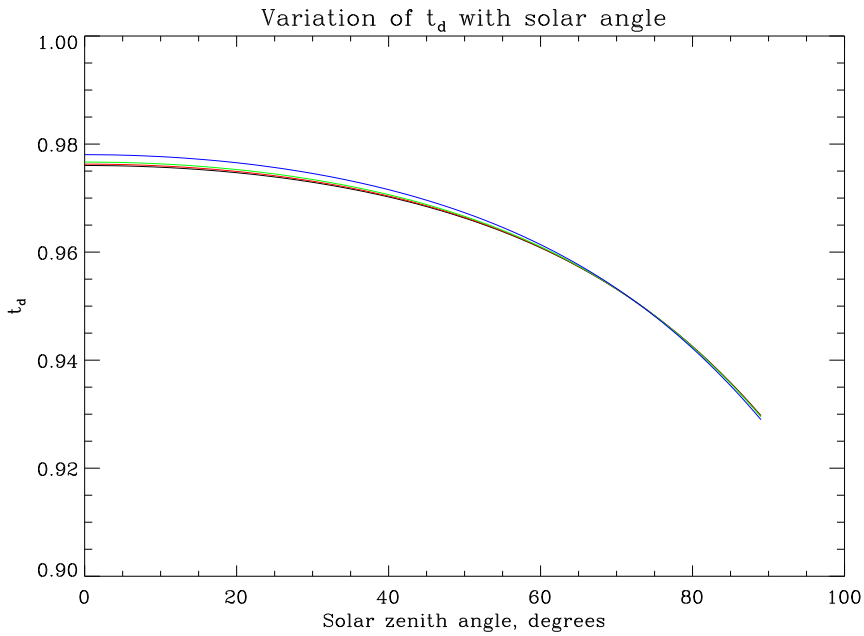

Figure 5: Downwelling transmittance coefficient t_d as a function of solar zenith angle θ_s. Black is 550 nm, red 660 nm, green 870 nm and blue 1.6 μm.

The variation of t_d with θ_s is shown in Figure 5. The range of variability is not high, and there is a comparatively weak dependence on wavelength. The integration described in Equation 19 is computationally demanding, so a lookup table is generated at 1° intervals and linearly interpolated.

The counterpart of t_d, r_d is the reflectance coefficient for downwelling radiation. This is different from the Fresnel coefficient described in the previous chapter, as integration is carried out over all angles (as opposed to only considering those geometries which result in light reaching an observer at zenith angle θ_v). It is not necessary to explicitly calculate r_d for this algorithm.

4.1.2 Upwelling transmittance coefficient, t_u

Analagous to t_d, the parameter t_u represents the transmittance of rays from below the water surface up to the observer at zenith angle θ_v. It is calculated as follows:

$$t_u = 1 - \int_0^{2\pi} \int_0^{\pi/2} R_{wa}(\theta_v, \theta_u, \phi) \cos(\theta_u) \sin(\theta_d) \, d\theta_u \, d\phi \tag{20}$$

Calculation is slightly more complicated than for t_d, and the relevant geometry is shown in Figure 6. The angle θ_u represents the zenith angle *in the water* of an upwelling light beam refracted to the observer in the air at θ_v. The coefficient R_{wa} is the Fresnel coefficient for a beam of zenith angle θ_u coming up from the water and refracted to θ_v: hence, θ_u cannot simply be used directly in Equation 12 as we instead need to know the angle x this incoming beam makes with the water-air interface, which can be obtained as follows:

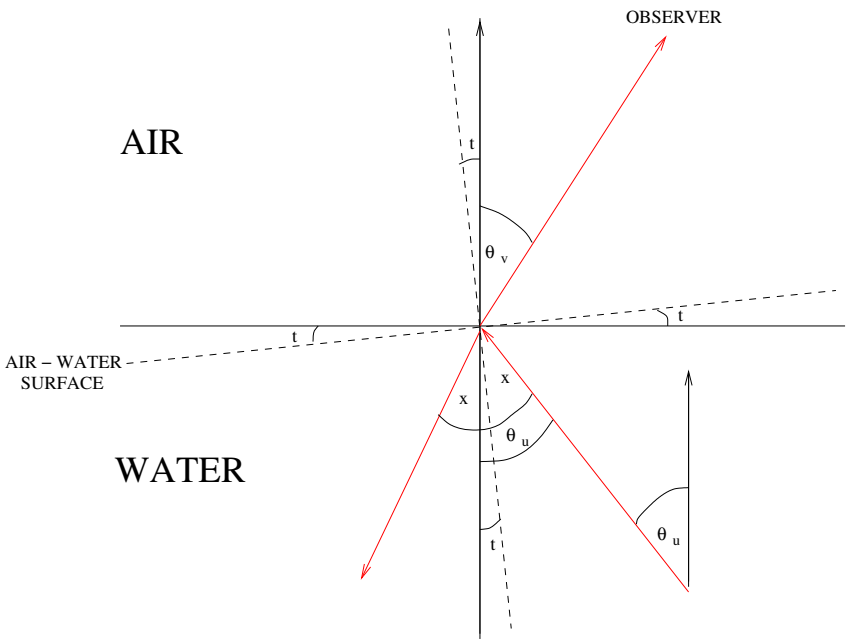

Figure 6: Geometry system defined for calculation of t_u. Solid black lines are the verticals zenith is measured against, while dotted are the inclincation and normal to the true sea surface. Red lines represent paths of light rays.

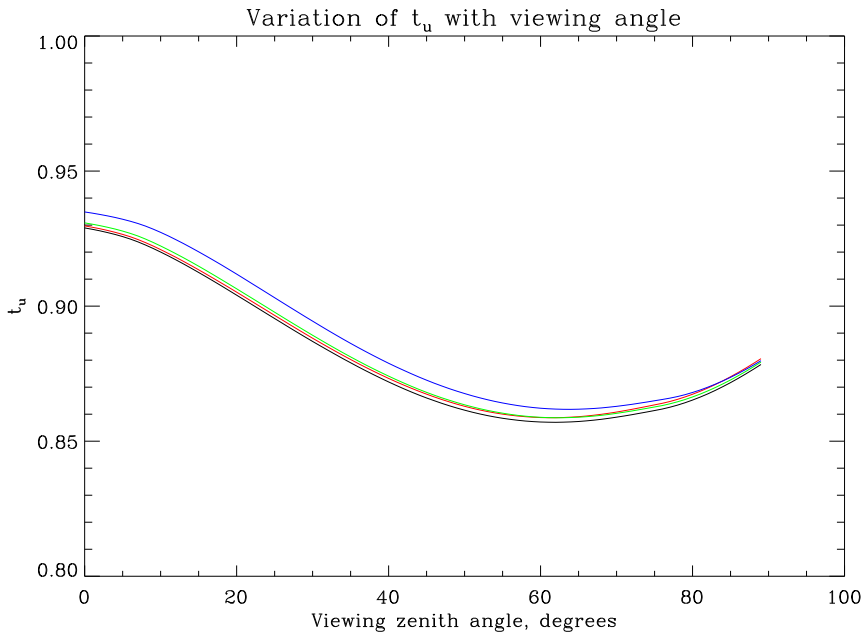

Figure 7: Upwelling transmittance coefficient t_u as a function of instrument zenith angle θ_v. Black is 550 nm, red 660 nm, green 870 nm and blue 1.6 μm.

$$\tan(x) = \frac{1}{\frac{n_{water}}{n_{air}\sin(\theta_v+\theta_u)} - \cot(\theta_v+\theta_u)} \tag{21}$$

Equation 12 may then be used to calculate R_{wa} using x in place of θ_s, $(\theta_v+\theta_u-x)$ in place of θ_v and ϕ for ϕ_r. Care must also be taken when using Equation 11 to calculate ω' as light is travelling from water to air, rather than air to water: ω and ω' are effectively interchanged.

Figure 7 shows the variation of t_u with θ_v. Again, variability is small with both angle and wavelength, so a lookup table has been generated and is interpolated during use.

4.1.3 Mean upwelling reflectance coefficient, $\overline{r_u}$

The final geometric term $\overline{r_u}$ is the mean reflectance coefficient for upwelling radiance at the water-air boundary, and is defined as follows:

$$\overline{r_u} = 1 - \int_0^{\pi/2} t_u(\theta_v)\cos(\theta_v)\sin(\theta_v)\, d\theta_v \tag{22}$$

Rather than calculate this explicitly, Vermote et al. [1997] adopt a constant value of 0.485 based on values obtained by Austin [1974]. This is done as calculation of r_u is computationally expensive, the value does not vary greatly with conditions and, as will be discussed in the next section, the generally low values R_w takes means that ρ_{ul} calculated from Equation 18 is not affected by small changes in r_u. Therefore, it is suggested that the value of 0.485 also be adopted here.

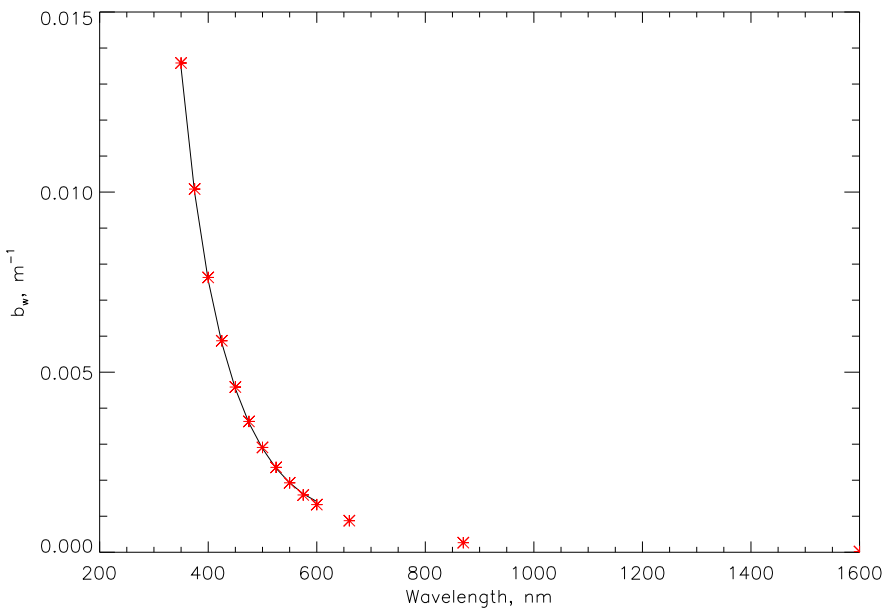

Figure 8: Variation of the molecular scattering coefficient for typical seawater b_w (m^{-1}) with wavelength. The black line shows values from Morel [1974] and red points the predicted values based on the relationship discussed in that paper, out to 1.6 μm.

4.1.4 Water body reflectance, R_w

Perhaps the most important of terms, R_w depends on the optical properties of the water. It is known as the water body reflectance, and is defined as the ratio of upwelling radiance from just below the surface to downwelling radiance just above it as follows:

$$R_w = \frac{E_u(\lambda)}{E_d(\lambda)} \tag{23}$$

The method of calculation is based on the method presented first in Morel and Prieur [1977], and further developed and discussed on many occassions (for example in Morel [1988] or Morel and Gentili [1991]). R_w is calculated from the optical properties of the water as follows:

$$R_w = f\frac{b_b(\lambda)}{a(\lambda)} \tag{24}$$

This equation describes the colour of the water as the ratio of the total backscattering coefficient $b_b(\lambda)$ to the absorption coefficient $a(\lambda)$, multiplied by some factor f.

A more thorough treatment can be given to the absorption coefficient of water than the approximation made previously. The total absorption coefficient a of seawater can be thought of as the sum of the absorption due to pure water, a_w (as in Equation 17), and that due to phytoplankton pigments $a_{ph}C$, where a_{ph} is the specific absorption coefficient of the pigments in m^2 mg^{-1} and C their concentration in mg m^{-3}:

Wavelength λ	Absorption coefficient of water a_w, m^{-1}	Specific absorption coefficient of pigment a_{ph}, m^2 mg^{-1}
550 nm	0.0448	0.0009
675 nm	0.425	0.0182
875 nm	5.65	0.0
1.6 μm	672	0.0

Table 3: Absorption coefficient a_w (m^{-1}) for pure water, and specific absorption coefficients of chlorophyll a_{ph} (m^2 mg^{-1}), at AATSR visible channel wavelengths.

$$a(\lambda) = a_w(\lambda) + a_{ph}(\lambda C) \tag{25}$$

Pigment coefficients are taken from Bidigare et al. [1990] for 550 nm and 660 nm. Values for longer wavelengths are unavailable and assumed to be zero: due to the large absorption coefficient of water, however, any contribution from pigments at these wavelengths is likely to be insignificant. Values of these coefficients are tabulated in Table 3.

The term $b_b(\lambda)$ represents the total backscattering coefficient, defined as follows:

$$b_b(\lambda) = b_{bw}(\lambda) + b_{bp}(\lambda) \tag{26}$$

This equation simply states that the total backscattering coefficient b_b is the sum of backscattering due to molecules, b_{bw}, and particles, b_{bp}. These terms may be further parametrised; firstly, b_{bw} may be represented as $b_w/2$ (molecular scattering is forward-back symmetric so the backscatter coefficient b_{bw} is half of the molecular scattering coefficient b_w). Secondly, scattering due to particles may be regarded as the product of the particle backscattering probability $\tilde{b}_b$ and particle backscattering coefficient b, leading to Equation 27:

$$b_b(\lambda) = \frac{1}{2} b_w(\lambda) + \tilde{b}_b(\lambda) b \tag{27}$$

Values for b_w for pure water from 380 nm to 700 nm were given by Morel and Prieur [1977]. An earlier paper by one of the authors, Morel [1974], tabulated values from 350 nm to 600 nm for both pure water and typical seawater. He noted that the data fit a power law with a dependence on $\lambda^{-4.32}$, with seawater scattering around 1.30 times as much as pure water. This relationship has been used to extrapolate this data to the 660 nm, 870 nm and 1.6 μm channels. The values obtained for b_w are 1.93×10^{-3} m^{-1} at 550 nm, 8.77×10^{-4} m^{-1} at 660 nm, 2.66×10^{-4} m^{-1} at 870 nm and 1.91×10^{-5} m^{-1} at 1.6 μm.

Figure 8 shows the tabulated and computed data. The relationship seems to slightly underpredict b_w at longer wavelengths, so it is thought that the extrapolated values are underestimates. The value predicted for 660 nm is, however, in good agreement with that given for pure water at 660 nm in Morel and Prieur [1977] multiplied by the aforementioned factor of 1.30, which is encouraging. Another point to note is that b_w is generally small (both in absolute terms and when compared to $\tilde{b}_b$) at longer wavelengths, meaning any error in this extrapolation is likely minor in terms of influence

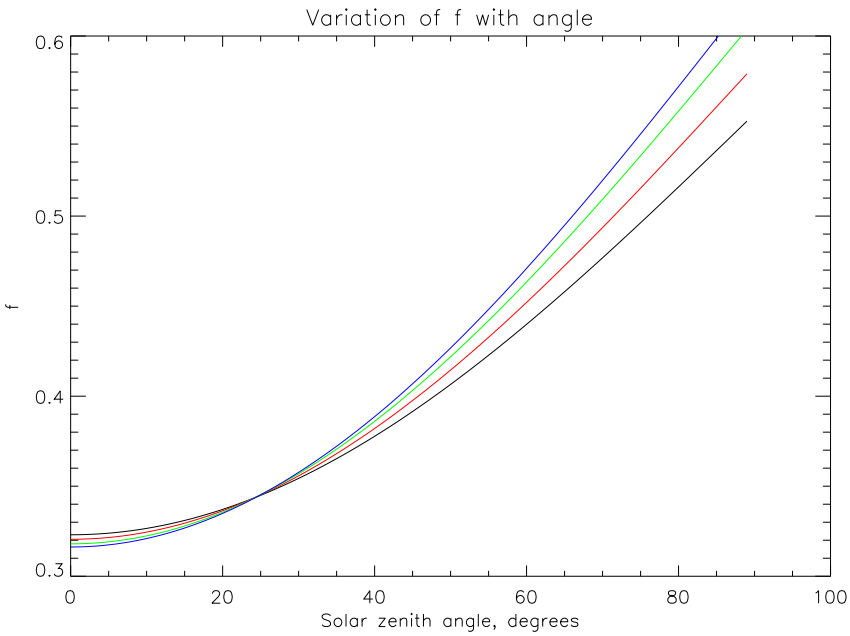

Figure 9: Variation of f with solar zenith angle and backscattering ratio η_b, based on a pigment concentration of 0.3 mg m^{-3}. The black line shows values for 550 nm, red for 660 nm, green for 870 nm and blue for 1.6 μm.

on R_w.

The second parameter in Equation 26, $\tilde{b}_b(\lambda)$, is the backscattering probability: the ratio of the backscattering to scattering coefficients of the pigments. It is related to the total concentration C of chlorophyll a and pheophytin a, measured in mg m^{-3}, and wavelength λ, measured in nm, by the following expression:

$$\tilde{b}_b(\lambda) = 0.002 + 0.02(0.5 - 0.25\log_{10}C)\frac{550}{\lambda} \tag{28}$$

The final term in the backscatter component of Equation 26, b is calculated from the following simple formula:

$$b = 0.3C^{0.62} \tag{29}$$

The relationship between b and C was derived by Morel [1988] for data at 550 nm; the wavelength dependence of particle backscattering is taken into account by the λ^{-1} factor in Equation 28. It should be noted that although parametrised in terms of C, the models were developed to account for scattering from suspended matter as well as pigment.

Morel and Prieur [1977] initially gave f a value of 0.33. Subsequent work has found it to depend on the solar geometry and the optical properties of water, leading to the development of several parametrisations. The method used here was put forward by Morel and Gentili [1991], stated to be accurate within 1.5% in for solar zenith angles smaller than 70°. It relates f to the proportion of

C, mg m^{-3}	550 nm	660 nm	870 nm	1.6 μm
0.1	1.73×10^{-2}	1.24×10^{-3}	6.04×10^{-5}	2.79×10^{-7}
1.0	3.62×10^{-2}	2.97×10^{-3}	1.66×10^{-4}	8.73×10^{-7}
10.0	7.74×10^{-2}	6.85×10^{-3}	4.17×10^{-4}	2.48×10^{-6}

Table 4: Water body reflectance R_w at AATSR visible wavelengths and pigment concentrations C. The solar zenith angle was taken to be 30°.

backscattering due to water molecules $\eta_b = b_{bw}/b_b$, and μ_s, the cosine of the solar zenith angle, as follows:

$$f = 0.6279 - 0.2227\eta_b - 0.0513\eta_b^2 + (-0.3119 + 0.2465\eta_b)\mu_s \tag{30}$$

Assuming a pigment concentration of 0.3 mg m^{-3}, representative η_b values are approximately 0.32 at 550 nm, 0.20 at 660 nm, 0.09 at 870 nm and 0.01 at 1.6 μm. The resultant variation of f is depicted in Figure 9, revealing a weak dependence on wavelength and a stronger dependence on solar angles. From this it can be seen that according to this parametrisation the constant value of 0.33 for f would in most cases be an underestimate.

The above equations allow computation of R_w at varying representative pigment concentrations, a selection of which are tabulated in Table 4. The strong dependence on both λ and C should be noted. It is also important to remember that the values for 870 nm and 1.6 μm are potentially less accurate, given b_w are possibly underestimates and a is greater than 1, meaning Equation 24 is less valid. Finally, use of Equation 17 instead of including effects of pigments (which will increase absorption) means the a values are likely underestimates, meaning R_w may be an overestimate.

4.2 Magnitude of contribution

The contribution ρ_{ul} is dominated by the shape of R_w, and is shown in Figure 10. At the shorter wavelengths it is of the order of $10^{-2} - 10^{-3}$, and is likely equal to or larger than other contributions to ρ. Hence knowledge of the true pigment concentration C is essential to accurately judge the magnitude of the contribution to the total reflectance. As it shows a stronger wavelength dependence than ρ_{wc} and ρ_{gl}, the spectral shape of the surface (which is constrained by the AATSR retrieval, and therefore more important to model than the absolute magnitude of ρ) will be largely determined by ρ_{ul}.

At longer wavelengths the contribution is low. For the 1.6 μm channel it should be safe to neglect the underlight contribution altogether, given that over the range of typical pigment concentrations it is calculated to be lower than the minimum increment used in the AATSR retrieval. The 870 nm contribution is also small, though may still be important in regions with low wind (hence a small ρ_{wc} and ρ_{gl}).

4.3 Uncertainties

The major uncertainties associated with ρ_{ul} are as follows:

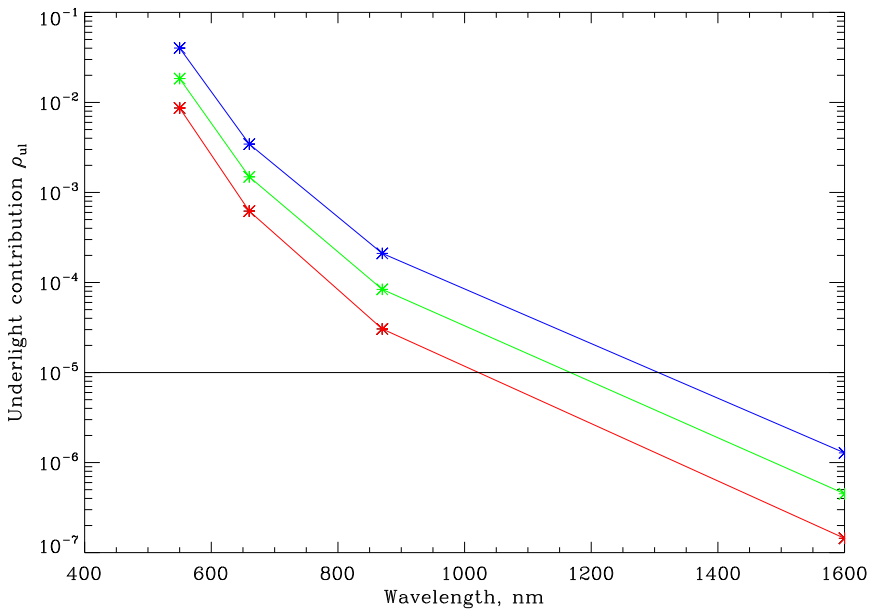

Figure 10: Variation of ρ_{ul} with wavelength, with points at the AATSR visible channel positions. The satellite zenith angle is taken as 10° and the solar zenith angle as 10°. Red points are for a pigment concentration C of 0.1 mg m^{-3}, green for 1 mg m^{-3} and blue for 10 mg m^{-3}. The line across $\rho_{ul} = 10^{-5}$ shows the minimum increment of surface reflectance for the AATSR retrieval.

- The scheme presented by Vermote et al. [1997] for finding R_w refers only to Case I waters. Austin [1974] and Morel and Prieur [1977] have discussed water of other types; a general method for Case II green waters or purely blue waters could be developed. In different water types the parametrisation relating the total scattering to concentration of pigments may not hold, as the ratio of suspended particles to pigments, used when deriving the parametrisation, may differ.

- Calculation of water absorption a should be improved by considering effects of suspended particles, as well as just pigments: this would lead to an increase in a, hence smaller R_w and ρ_{ul}. Furthermore, the assumption of zero absorption by pigments at the longer wavelengths should be tested.

- A knowledge of global pigment concentrations is necessary. The range of both spatial and temporal variability are important, as these will strongly affect the sea surface spectral shape. One possibility involving this would be to attempt to retrieve pigment concentration as opposed to surface reflectance, and assume the foam and specular reflectance terms are well-known. Allowing a retrieval of pigment concentration might determine whether the algorithm is able to cope with Case II waters (typically coastal, where high concentrations of pigment may be expected) or very blue waters (where a very low concentration is expected and water molecular scattering predominates).

4.4 Comparison with current algorithm

The current algorithm does not account for underlight.

5 Some preliminary results

5.1 Retrieved parameters

The new algorithm was applied on a scene tested over the past year during the development of the forward view and dual-view retrievals, at 10 km by 10 km resolution. An assumed pigment concentration of 0.5 mg m^{-3} was used as a rough value, based on inspection of a chlorophyll a map derived from SeaWIFS data. The parameters t_d and t_u were looked up for each pixel from values previously calculated for similar angles. For the dual-view retrieval, retrieved aerosol and surface properties are displayed in Figure 11 for new and old surface models.

5.1.1 A note on treatment of reflectance

The current ORAC algorithm calculates a directional reflectance, and converts it to an equivalent Lambertian reflectance before use in the retrieval (although the method used to do so is not clear). This new surface model, strictly speaking, calculates a directional reflectance rather than a Lambertian reflectance. The treatment of the surface by the aerosol forward model currently assumes a Lambertian surface and calculates accordingly. Additionally, the dual-view retrieval does not give a true Lambertian treatment to the surface (as two surface reflectances are retrieved, while for a Lambertian surface these would be identical) but it also does not give a true bidirectional reflectance (as the forward model is set up for a Lambertian surface).

Current work by G. Thomas involves setting up ORAC to use a full BRDF surface description; this will enable a better comparison of the merits of this sea surface model. Essentially, the directional reflectance produced is integrated over viewing angles to produce a black-sky albedo, which is then integrated over solar angles to obtain a white-sky albedo (which is the Lambertian albedo). The forward model must be changed as these black-sky and white-sky albedos are not the same.

5.1.2 Effective radius and surface albedo

The previous algorithm often led to very low effective radii, and a low surface albedo, being retrieved over large parts of the ocean. It was surmised that these two were linked, with a low surface albedo leading to smaller effective radius (as small particles more efficiently scatter light in the backward direction). The *a priori* component of cost was consequently comparatively large, as the effective radius was far from the *a priori*. The results above show more reasonable values for effective radius; surface albedo tends to be higher. The streaks in the surface albedo plots are attributable to being near the sun-glint region.

5.1.3 Single-view retrieval comparisons

Figures 12 and 13 depict comparisons of retrieved properties for the single-view retrievals using the algortihm presented here. In both cases, the correlation is far from perfect. A more accurate model of the sea surface would be expected to improve the agreement between nadir and forward-view retrieved values, as it would decrease one source of bias in the retrievals.

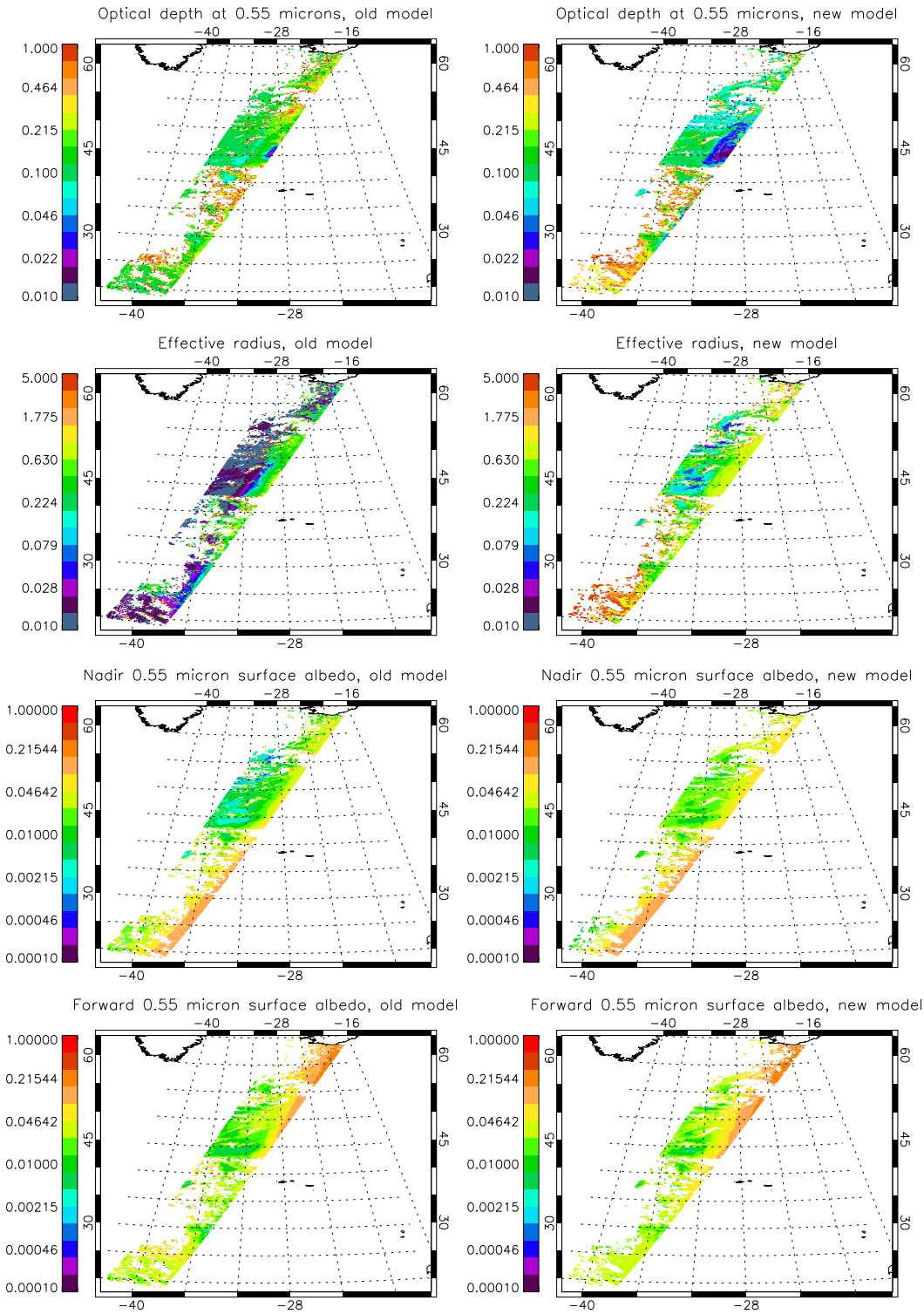

Figure 11: Retrieved aerosol and surface properties for the test scene using the model currently in use in the ORAC retrieval (left) and the sea surface albedo model described here (right figures).

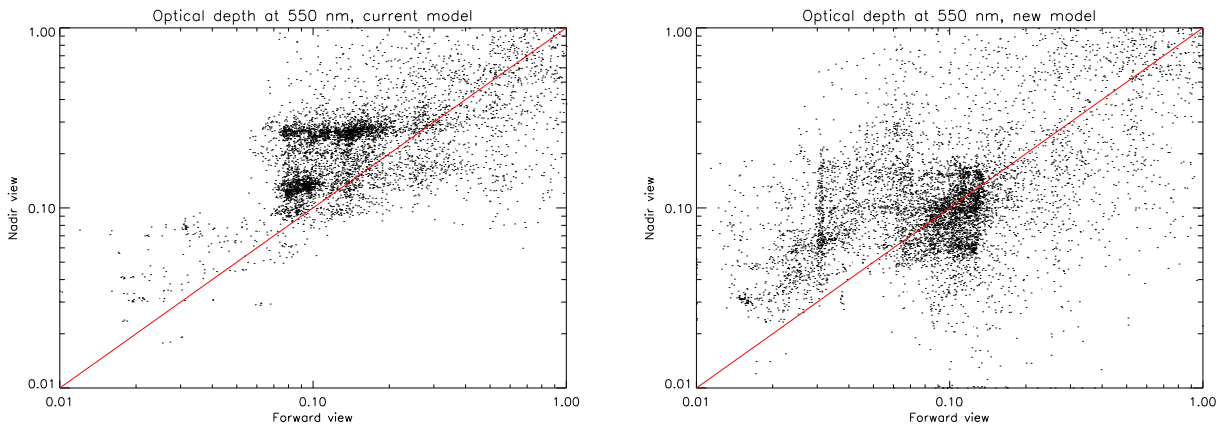

Figure 12: Pixel-by-pixel comparison of retrieved optical depth for single-view retrievals using the current sea surface albedo model (left) and the new one described here (right).

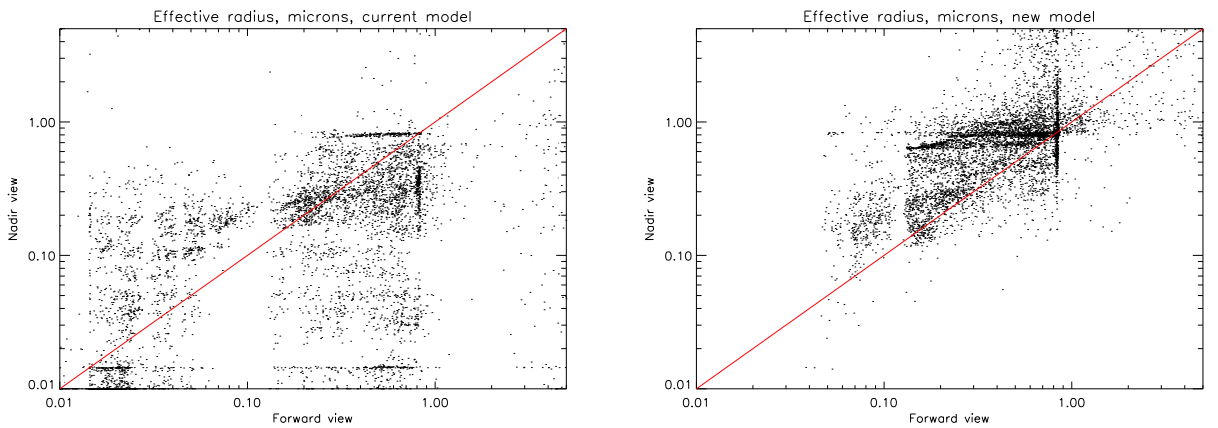

Figure 13: Pixel-by-pixel comparison of retrieved effective radius for single-view retrievals using the current sea surface albedo model (left) and the new one described here (right).

The lines visible along the points in Figure 13 are probably indicative of the retrieval not performing well for that particular view, and sitting on the *a priori* value or a lookup table point. This behaviour is generally not observed in a dual-view retrieval.

It is expected that dual-view retrieved aerosol properties would be intermediate between the forward and nadir single-view retrieved quantities; this was seen for some pixels using the old algorithm, and is seen for a higher proportion with the new algorithm. Like the previous scheme, dual-view retrieved quantities tend to have smaller error estimates than the single-view ones, and have a comparable retrieval cost.

5.2 Residuals

One area in which the current algorithm compares unfavourably with the old is in the distribution of residuals. Ideally, thse would be Normally distributed with a mean of 0. Residuals in the new algorithm tend not to be as favourably distributed as before–particularly at 550 nm, as is visible in Figure 14. For comparison, residuals using the standard ORAC scheme are shown in Figure 15.

The distribution at 550 nm may be due to the choice of pigment concentration C for calculation of ρ_{ul}, which will dominate the surface albedo and spectral shape at the shorter wavelengths. Use of a more accurate value for C should hopefully minimise any bias in residuals due to an incorrect *a priori* model. Running the retrieval using a much lower assumed pigment concentration in an AATSR scene thought to be over a very blue ocean may demonstrate this, if this bias disappears and retrieval comparisons are favourable.

5.3 Comparative cost and other diagnostics

The cost of the retrieval using old and new sea surface schemes is shown in Figure 16. Among pixels with low cost it appears that the new scheme has an edge. A more accurate pigment concentration would hopefully improve the retrieval performance, decreasing the cost further in the new scheme. Visual inspection of maps of cost such as Figure 17 more directly show the improved performance of the new method, particularly in terms of geometric bias. The decrease in the *a priori* component of cost, as a result of more reasonable effective radii now being retrieved in the west of the image, is clearly visible.

Figure 18 also shows that, in general, the new sea surface model leads to faster convergence of the retrieval as compared to the model currently in use.

A final point to note is the number of retrievals which successfully converge: for this test scene, the proportion is very similar for the new and old schemes. Were it significantly lower for the new scheme, that would be an indication that the method may not be so applicable for all conditions.

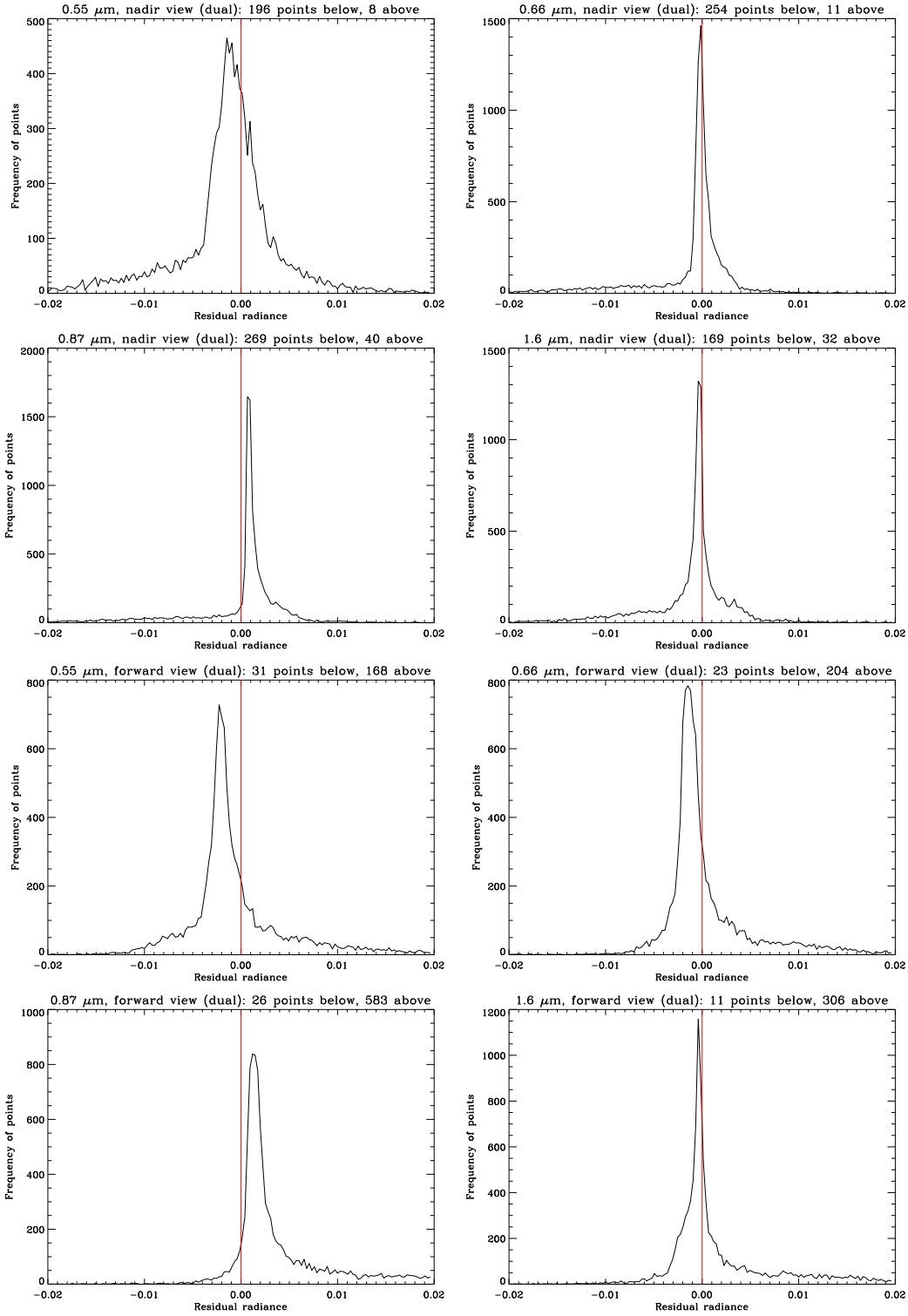

Figure 14: Residuals on radiance for the instrumental channels used, for dual-view nadir (top four graphs) and forward (bottom four graphs) retrievals, using the sea surface albedo model described here. The number of points falling above and below these ranges is noted in each graph's title.

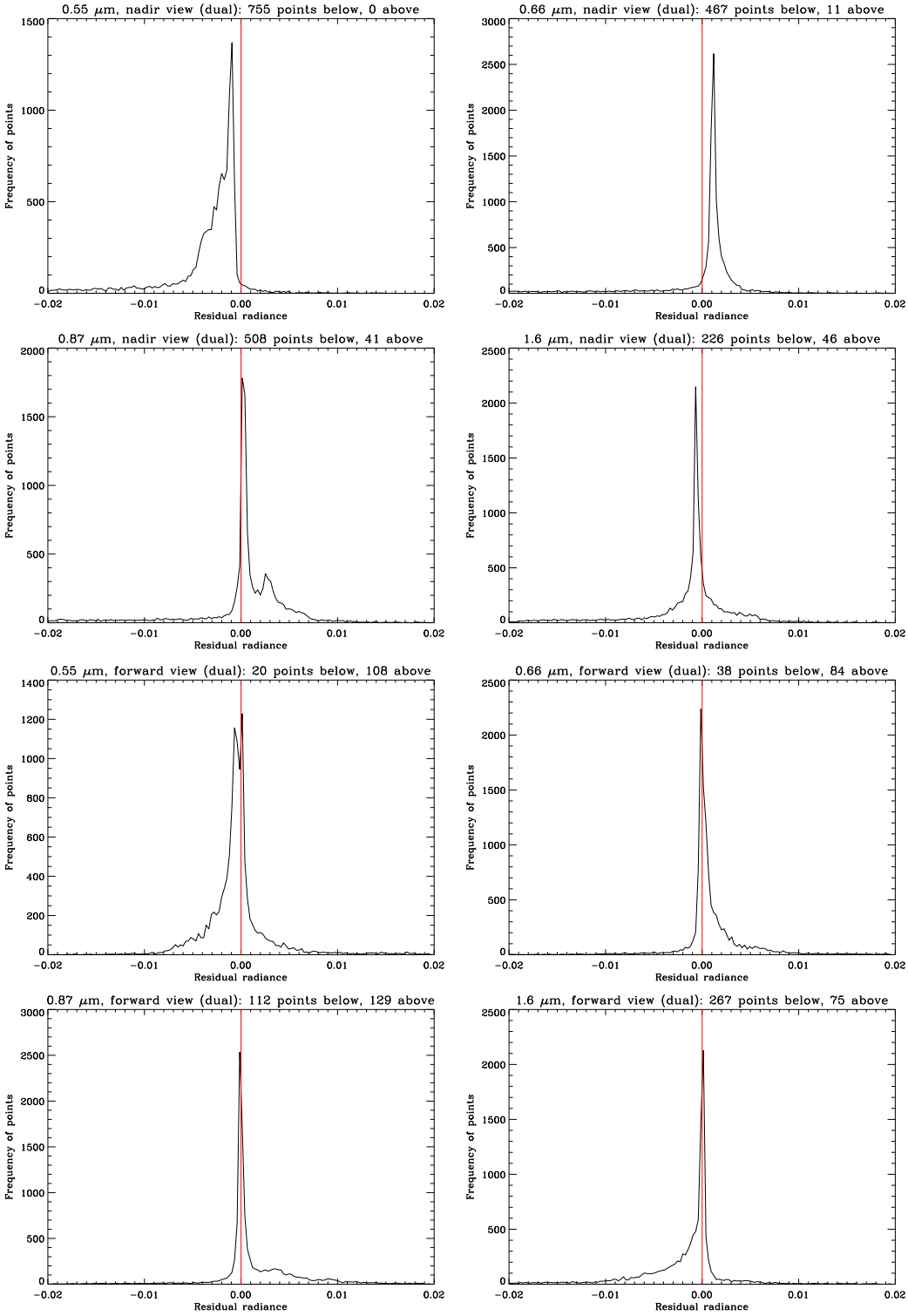

Figure 15: Residuals on radiance for the instrumental channels used, for dual-view nadir (top four graphs) and forward (bottom four graphs) retrievals, using the current ORAC sea surface albedo scheme. The number of points falling above and below these ranges is noted in each graph's title.

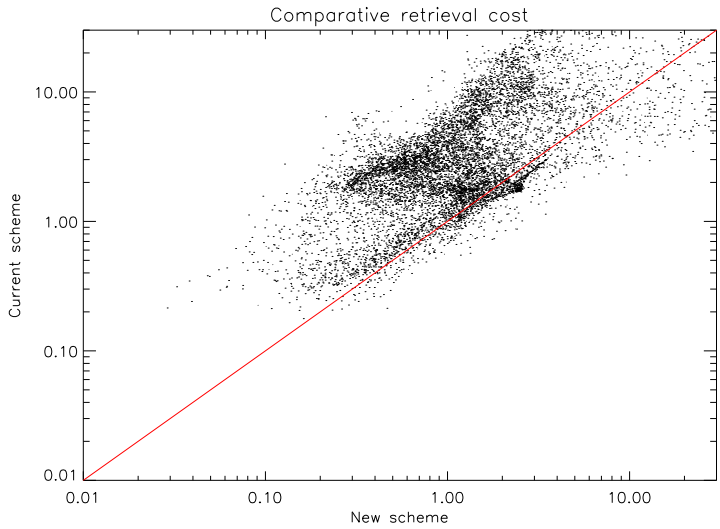

Figure 16: Pixel-by-pixel comparison of retrieval cost for the dual-view retrieval under the new and old sea surface models.

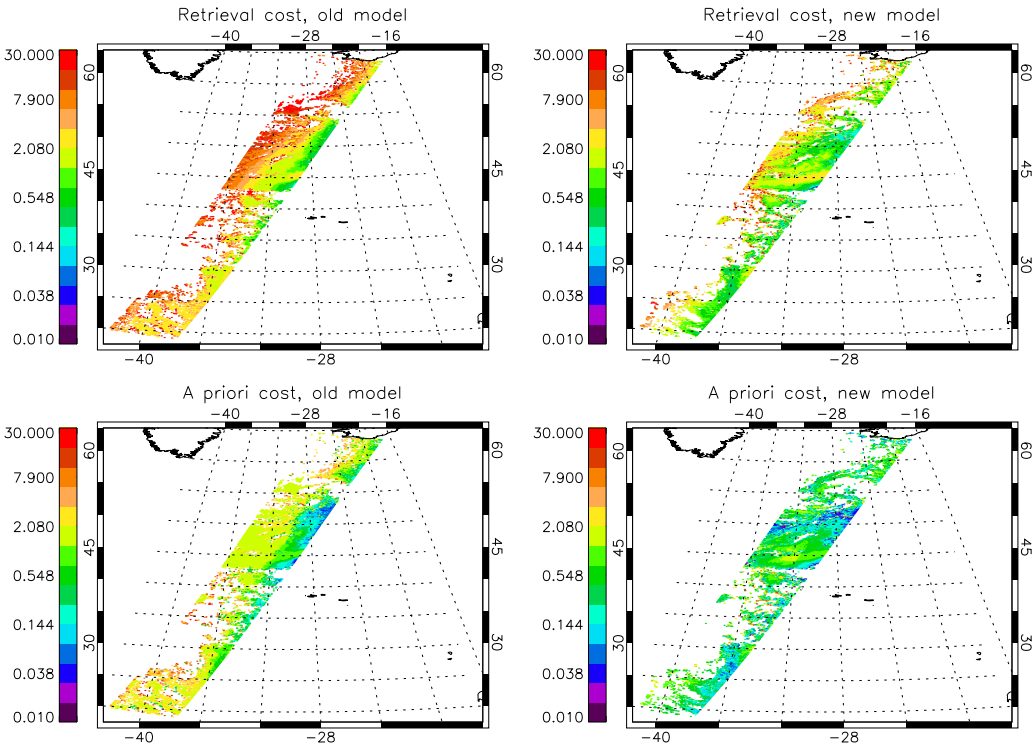

Figure 17: Map-based comparison of retrieval cost for the dual-view retrieval under the old (left) and new (right) sea surface models, showing both total cost and the *a priori* component.

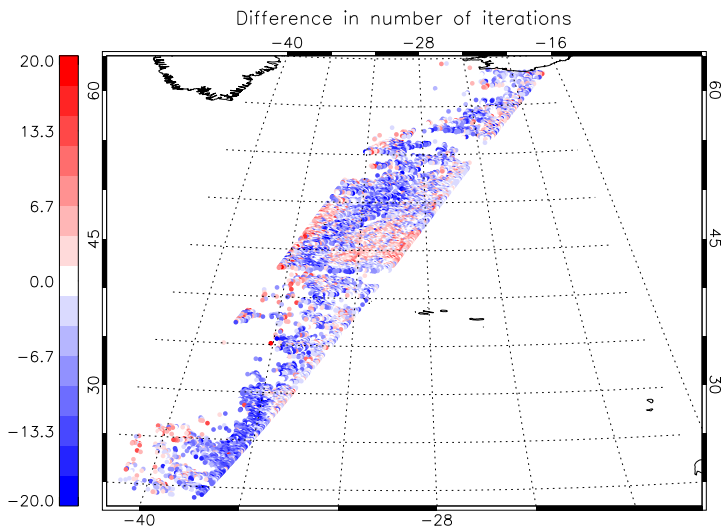

Figure 18: Map-based comparison of the difference between the number of iterations taken for the retrieval to converge under the new sea surface model, as opposed to the one currently in use. Blue areas are where the new model converges more rapidly. Results for the dual-view retrieval.

References

Anguelova, M. and Webster, F. [2006], 'Whitecap coverage from satellite measurements: A first step toward modeling the variability of ocean whitecaps', *J. Geophys. Res.* **111**.

Austin, R. W. [1974], 'The remote sensing of spectral radiance from below the ocean surface.', *Optical Aspects of Oceanography, N. G. Jerlov and E. S. Nielsen, Eds., Academic Press* pp. 317–344.

Bidigare, R. R., Ondrusek, M. E., Morrow, J. H. and Kiefer, D. A. [1990], 'In vivo absorption properties of algal pigments', *SPIE Ocean Optics X* **1302**, 290–302.

Born, M. and Wolf, E. [1975], *Principles of Optics*, Pergamon.

Cox, C. and Munk, W. [1954*a*], 'Measurement of the roughness of the sea surface from photographs of the Sun's glitter', *J. Opt. Soc. Am.* **44**, 838–850.

Cox, C. and Munk, W. [1954*b*], 'Statistics of the sea surface derived from Sun glitter', *J. Mar. Res.* **13**, 198–227.

Frouin, R., Schwindling, M. and Deschamps, P.-Y. [1996], 'Spectral reflectance of sea foam in the visible and infra-red: In situ measurements and remote sensing implications', *J. Geophys. Res.* **101**(C6), 14361–14371.

Hale, G. M. and Querry, M. R. [1971], 'Optical constants of water in the 200-nm to 200-μm wavelength region', *Appl. Opt.* **12**(3), 555–563.

Koepke, P. [1984], 'Effective reflectance of oceanic whitecaps', *Appl. Opt.* **23**(11), 1816–1824.

Monahan, E. C. and Muircheartaigh, I. O. [1980], 'Optimal power-law description of oceanic whitecap coverage dependence on wind speed', *J. Phys. Oceanogr.* **10**, 2094–2099.

Morel, A. [1974], 'Optical properties of pure water and pure sea water.', *Optical Aspects of Oceanography, N. G. Jerlov and E. S. Nielsen, Eds., Academic Press* pp. 1–24.

Morel, A. [1988], 'Optical modeling of the upper ocean in relation to its biogenous matter content (Case I waters)', *J. Geophys. Res.* **93**(C9), 10749–10768.

Morel, A. and Gentili, B. [1991], 'Diffuse reflectance of oceanic waters: its dependence on Sun angle as influenced by the molecular scattering contribution', *Appl. Opt.* **30**(30), 4427–4438.

Morel, A. and Prieur, L. [1977], 'Analysis of variations in ocean color', *Limnol. Oceanogr.* **22**(4), 709–722.

Nicolas, J.-M., Deschamps, P.-Y. and Frouin, R. [2001], 'Spectral reflectance of oceanic whitecaps in the visible and infra-red: Aircraft measurements over open ocean', *Geophys. Res. Lett.* **28**(23), 4445–4448.

Sidran, M. [1981], 'Broadband reflectance and emissivity of specular and rough water surfaces', *Appl. Opt.* **20**(18), 3176–3183.

Vermote, E. F., Tanré, D., Deuzé, J. L., Herman, M. and Morcrette, J.-J. [1997], 'Second Simulation of the Satellite Signal in the Solar Spectrum, 6S: An Overview', *IEEE Trans. Geosci. Remote Sens.* **35**(3), 675–686.